Chinese Chemical Letters 36 (2025) 109695

Contents lists available at ScienceDirect

Chinese Chemical Letters

journal homepage: www.elsevier.com/locate/cclet

$BiVO_4$ as a precatalyst for CO_2 electroreduction to formate at large current density

Longsheng Zhan[1], Yuchao Wang[1], Mengjie Liu[1], Xin Zhao, Danni Deng, Xinran Zheng, Jiabi Jiang, Xiang Xiong, Yongpeng Lei*

State Key Laboratory of Powder Metallurgy, Central South University, Changsha 410083, China

ARTICLE INFO

Article history:
Received 21 January 2024
Revised 18 February 2024
Accepted 26 February 2024
Available online 1 March 2024

Keywords:
CO_2 electroreduction
Bismuth vanadate
Formate
Oxygen vacancies
Large current density

ABSTRACT

The large current density of electrochemical CO_2 reduction towards industrial application is challenging. Herein, without strong acid and reductant, the synthesized $BiVO_4$ with abundant oxygen vacancies (O_{vs}) exhibited a high formate Faradaic efficiency (FE) of 97.45% (-0.9 V) and a large partial current density of -45.82 mA/cm^2 (-1.2 V). The good performance benefits from the reconstruction of $BiVO_4$ to generate active metal Bi sites, which results in the electron redistribution to boost the OCHO* formation. In flow cells, near industrial current density of 183.94 mA/cm^2 was achieved, with the FE of formate above 95% from 20 mA/cm^2 to 180 mA/cm^2. Our work provides a facily synthesized $BiVO_4$ precatalyst for CO_2 electroreduction.

As one of the most attractive approaches to achieve carbon peaking and carbon neutralization, electrochemical CO_2 reduction reaction (CO_2RR) receives widespread attention [1–4]. Generally, products of CO_2RR can be divided into C_1 (CO, $HCOO^-$, *etc.*) [5–7] and C_{2+} (C_2H_4, C_2H_5OH, *etc.*) [8–11]. Technical and economic analysis indicates that formic acid/formate are the most valuable product, which are important industrial raw materials and fuels for fuel cells [12–14]. Compared with other metallic materials, such as Pd, In, and Sn, bismuth (Bi)-based materials are potential candidates due to the effective inhibition of competitive hydrogen evolution reaction during CO_2RR [15].

Recently, some modulation strategies have been applied to improve the performance of CO_2RR [16,17], such as the two-dimensional transformation [18], interface construction [19], defect engineering [20,21], and element doping [22]. For instance, catalyst reconstruction could effectively modulate the local electronic structure of active sites, which was beneficial for the adsorption and conversion of CO_2 molecules [23]. However, the reconstruction process of $BiVO_4$ with oxygen vacancies (O_{vs}) was rarely noted in electrocatalytic CO_2 reduction.

Herein, $BiVO_4$ was synthesized by a relatively simple process (no strong acids and strong reductant) (Table S1 in Supporting information). As a precatalyst, the optimized sample (BV-2) reconstructed into active metal Bi during the reaction process, which presented the maximum formate selectivity of 97.45% at −0.9 V and a large partial current density of −45.82 mA/cm^2 at −1.2 V. In two-electrode flow cells, the formate selectivity maintained ~95% from 20 mA/cm^2 to 180 mA/cm^2, and the maximum partial current density could reach 175.23 mA/cm^2 at 2.8 V.

As shown in Fig. 1a, a series of $BiVO_4$ (BV) were synthesized by a hydrothermal strategy. The difference among them is the amount of sodium dodecyl sulfonate (SDS) during prepared process. BV-0, BV-1, BV-2 and BV-3 were constructed *via* adding 0, 0.1, 0.2 and 0.3 g SDS, respectively. It is clear that there was no significant difference in the color of the series of samples as shown in Fig. S1. The X-ray diffraction (XRD) patterns in Fig. 1b showed that the phase of $BiVO_4$ was multiple crystal structures. BV-0, BV-1 and BV-2 were consistent with monoclinic $BiVO_4$ (m-$BiVO_4$, PDF#14–0688) and tetragonal $BiVO_4$ (t-$BiVO_4$, PDF#14–0133). When adding 0.3 g SDS, additional crystal phase ascribed to tetragonal structure (PDF#49–0198) in XRD of BV-3. The highest diffraction peak at 24.4° in XRD of BV-2 was corresponding to the $BiVO_4$ (200) tetragonal structure (PDF#14–0133). However, the highest diffraction peak at 28.9° of other samples was $BiVO_4$ (121), which was consistent with monoclinic structure (PDF#14–0688).

Fourier transform infrared (FT-IR) spectra (Fig. S2 in Supporting information) were aimed to explore the functional groups in $BiVO_4$. The strong peak of 749 cm^{-1} was assigned to the asymmetric stretching of VO_4^{3-}, revealing successful synthesis of $BiVO_4$ [24]. Raman spectra (Fig. 1c) were investigated to verify the struc-

* Corresponding author.
E-mail address: leiyongpeng@csu.edu.cn (Y. Lei).
[1] These authors contributed equally to this work.

https://doi.org/10.1016/j.cclet.2024.109695
1001-8417/

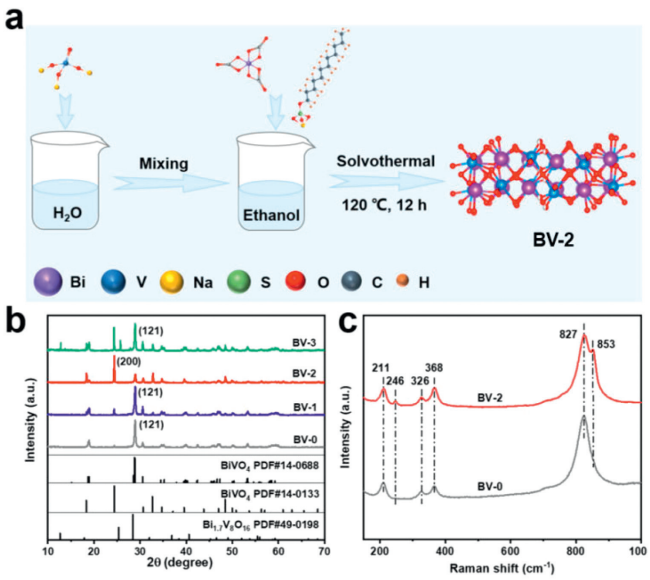

Fig. 1. (a) Schematic illustration for the synthesis of BV-2. (b) XRD patterns of different samples. (c) Raman results of BV-2 and BV-0.

ture of $BiVO_4$ [25]. The bands at 211, 326, 368 and 827 cm^{-1} were assigned to the vibrations of monoclinic $BiVO_4$ [26]. The additional shoulder band at 853 cm^{-1} was ascribed to the symmetric stretching mode of V-O band for tetragonal $BiVO_4$ [27]. It meant that the prepared samples were the mixed crystalline structure of $BiVO_4$, which was in compliance with XRD results. The band at 246 cm^{-1} of BV-2 was attributed to O_{vs}. We suppose that adding SDS could introduce O_{vs} in $BiVO_4$ [28].

To investigate the chemical valence states and compositions of BV species, the X-ray photoelectron spectroscopy (XPS) measurement was employed. The survey spectra were shown in Fig. S3 (Supporting information), indicating co-existences of Bi, V and O elements. As shown in Bi 4f XPS spectra (Fig. 2a), for BV-0, two peaks at 164.2 and 158.9 eV were corresponded to Bi $4f_{5/2}$ and Bi $4f_{7/2}$, respectively, implying the valence of Bi was +3. Compared with BV-0, characteristic peaks of BV-2 showed a slight shift to low binding energy. Moreover, two characteristic peaks of BV-2 in V 2p spectra also showed a slight shift (~0.1 eV) to low binding energy (Fig. S4 in Supporting information). As shown in Fig. 2b, the high-resolution O 1s XPS spectra were deconvoluted into three peaks with the lattice oxygen, surface hydroxyls and adsorbed oxygen, corresponding to the binding energies of 533, 530.9 and 529.4 eV, respectively. The surface hydroxyls (OH) were related to the dissociative adsorption of water with O_{vs}. BV-2 displayed more OH, indicating more O_{vs}, which were calculated based on the area of peaks (Table S2 in Supporting information) [29]. The slight shift of Bi 4f and V 2p XPS spectra, was possibly due to the different chemical environment caused by O_{vs}.

In order to further confirm the existence of O_{vs}, electron paramagnetic resonance (EPR) was employed (Fig. 2c). Paramagnetic signal at $g = 2.004$ was characteristics of O_{vs}. Compared to BV-0, the peak intensity of BV-2 was enhanced, which might improve the mobility of electrons. The crystal structure was disclosed by high-resolution transmission electron microscope (HRTEM). In Fig. S5 (Supporting information), BV-2 revealed lattices fringes with interatomic distance of 0.269 nm for the (112) plane of t-$BiVO_4$ and 0.308 nm for the (121) plane of m-$BiVO_4$. The interface (labeled by pink line) between t-$BiVO_4$ and m-$BiVO_4$ was observed. Meanwhile, BV-0 exhibited the (121) plane of m-$BiVO_4$ with lattices fringes of 0.308 nm (Fig. S6 in Supporting information). No planes of t-$BiVO_4$ were found. The energy dispersive spectra (EDS) elemental mapping images of BV-2 and BV-0 were presented in Fig. 2d and Fig. S7 (Supporting information). The results revealed the uniform distribution of Bi, V and O elements.

To evaluate the CO_2RR performance of electrocatalysts, H-type cells were applied with 0.5 mol/L $KHCO_3$ as electrolyte [30]. All the potential was referred to the reversible hydrogen electrode (RHE). The commercial Bi powder (C-Bi) with the size of 200 mesh was selected for comparison. Firstly, we tested the linear sweep voltammetry (LSV) curves at different saturated atmosphere (Ar and CO_2). The difference of curves indicated their CO_2 conversion capacity (Fig. S8 in Supporting information) [31]. As displayed by LSV curves in CO_2-saturated atmosphere in Fig. 3a, the current density of BV-2 sharply increased and markedly reached -49.16 mA/cm^2 at -1.2 V, which was larger than that of other samples. To figure out their activity and selectivity towards CO_2RR, the constant voltage electrolysis was carried out (Fig. S9 in Supporting information). $HCOO^-$ was the main products from CO_2RR for BV species (Fig. S10 in Supporting information). In Fig. 3b, the for-

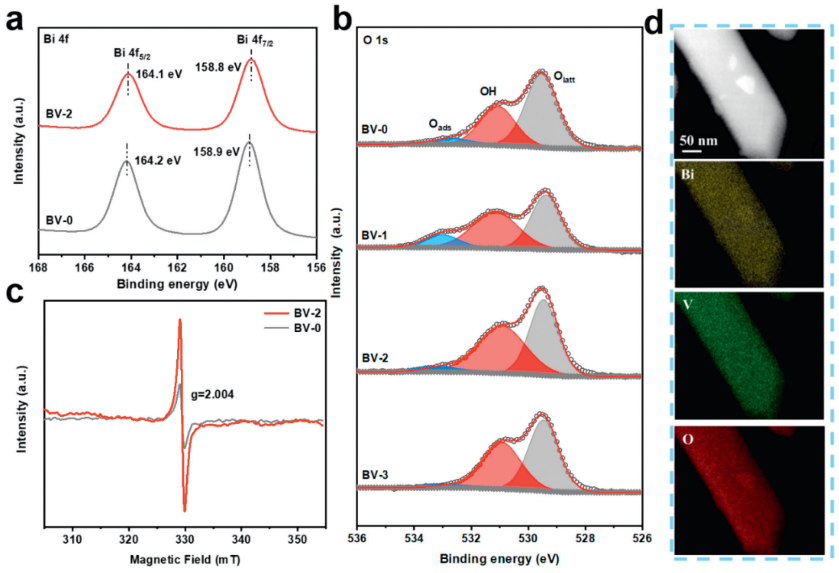

Fig. 2. (a) Bi 4f XPS results and (b) O 1s XPS results of different samples. (c) EPR spectra of BV-0 and BV-2. (d) EDS mapping images of BV-2.

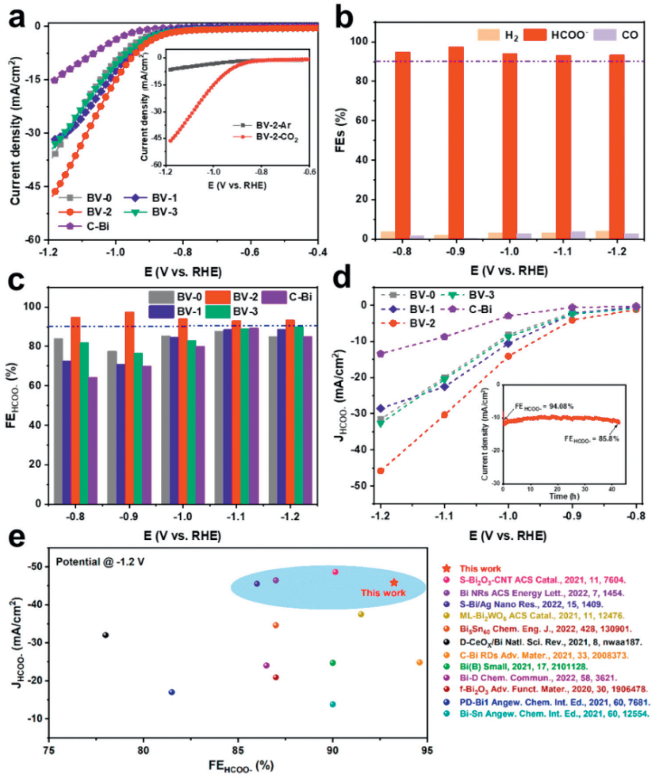

Fig. 3. (a) LSV curves of different samples at CO_2-saturated atmosphere, inset: LSV curves of BV-2 under different atmosphere. (b) FEs with different products of BV-2. (c) FE_{HCOO-}. (d) J_{HCOO-}, inset: the stability test of BV-2 at −1.0 V in H-type cells. (e) The performance comparison of up-to-date Bi-based catalysts for CO_2RR in H-type cells.

mate Faradaic efficiency (FE_{HCOO-}) of BV-2 was greater than 90% from −0.8 V to −1.2 V, which could arrive 97.45% at −0.9 V. Fig. 3c showed the comparison of FE_{HCOO-} with other samples (BV-0, BV-1, BV-3 and C-Bi), founding that BV-2 displayed the highest FE_{HCOO-} and widest voltage window. Also, BV-2 achieved a maximum J_{HCOO-} of −45.82 mA/cm^2@−1.2 V, while the J_{HCOO-} of C-Bi was −13.42 mA/cm^2@−1.2 V (Fig. 3d). BV-2 at −1.0 V could reach a stability of 40 h and FE_{HCOO-} of 85.8% (inset of Fig. 3d). Fig. 3e and Table S3 (Supporting information) gave a summary of up-to-date Bi-based catalysts for J_{HCOO-} in H-type cells. BV-2 outperformed most of reported electrocatalysts for CO_2RR.

In-situ Raman spectra were further investigated (Figs. 4a and b). As the electrolysis proceeded, Bi-Bi bands were appeared at 63 and 84 cm^{-1} [32]. It meant that BV-2 acted as a precatalyst. During the electrolysis process, BV-2 underwent surface reconstruction to produce metal Bi, which consisted with the XRD and XPS results of BV-2 after reaction (Figs. S11 and S12 in Supporting information). Then the peak at 1540 cm^{-1} was stronger with prolonged time, which could be assigned to asymmetric C–O stretching vibration of OCHO* intermediate [33]. The reconstruction process induced a redistribution of charges, promoting the conversion of CO_2 molecules. Then we explored the electrochemical active surface areas (ECSA), which was evaluated by the electric double-layer capacitance (C_{dl}) method (Fig. S13 in Supporting information) [34,35]. As shown in Fig. S14a (Supporting information), BV-2 had the larger C_{dl} with 1090 μF/cm^2 than other samples, corresponding to larger ECSA. Also, C_{dl} of BV-0 (497 μF/cm^2), BV-1 (585 μF/cm^2) and BV-3 (652 μF/cm^2) were greater than that of C-Bi (304 μF/cm^2). In Fig. S14b (Supporting information), the Tafel slope was ~178.1 mV/dec of BV-2, significantly lower than ~201.7 mV/dec for BV-0, indicating faster reaction kinetics [36,37].

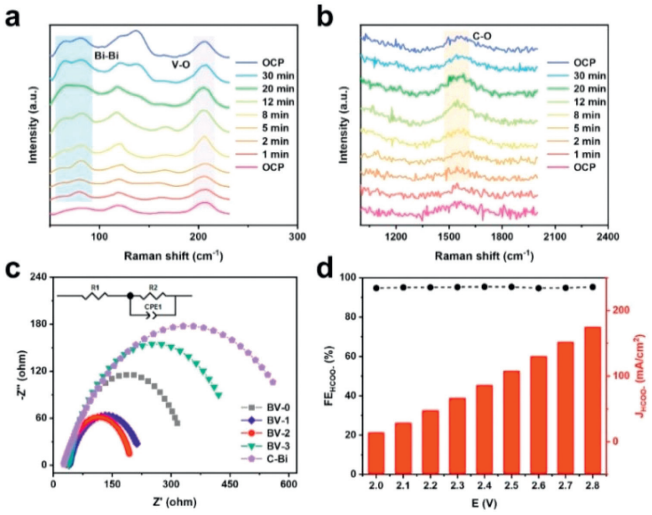

Fig. 4. (a, b) *In-situ* Raman spectra recorded at −1.0 V. (c) EIS measurement, (d) FE_{HCOO-} and J_{HCOO-} of BV-2 in flow cells.

The electrochemical impedance spectroscopy (EIS) was conducted. The EIS results and the corresponding equivalent circuit was presented in Fig. 4c. BV-2 demonstrated the smallest charge-transfer resistance than other contrast samples (Table S4 in Supporting information), enabling the largest current density of formate.

Furthermore, the CO_2RR performance in flow cells was evaluated [38]. Nickle foam was used as anode and BV-2 supported on gas diffusion layer was used as cathode. When changing the saturated atmosphere from Ar to CO_2, the current density in LSV curves was increased, indicating that excellent CO_2 activity (Fig. S15 in Supporting information) [39]. The maximum current density arrived 183.94 mA/cm^2 at 2.8 V, which was closed to industrial-scale current density [40]. The J_{HCOO-} of BV-2 could reach 175.23 mA/cm^2 at 2.8 V as well as the FE_{HCOO-} remain around 95% from 20 mA/cm^2 to 180 mA/cm^2 (Fig. 4d and Fig. S16 in Supporting information).

In summary, $BiVO_4$ with O_{vs} was constructed through a relatively simple synthesis approach, which acted as a precatalyst for CO_2RR. The BV-2 achieved high FE_{HCOO-}, large J_{HCOO-} of −45.82 mA/cm^2 (−1.2 V) in H-type cells and near industrial current density in flow cells.

Declaration of competing interest

The authors declare that they have no known competing financial interests or personal relationships that could have appeared to influence the work reported in this paper.

Acknowledgments

This work was financially supported by the Fundamental Research Funds for the Central Universities of Central South University (No. 2022ZZTS0579).

References

[1] Y.C. Wang, Q.C. Wang, J. Wu, et al., Nano Energy 103 (2022) 107815.
[2] Y.C. Wang, Y. Liu, W. Liu, et al., Energy Environ. Sci. 13 (2020) 4609.
[3] Y.F. Jia, F. Li, K. Fan, L.C. Sun, Adv. Powder Mater. 1 (2022) 100012.
[4] M.J. Liu, L.S. Zhan, Y.C. Wang, et al., J. Mater. Sci. Technol. 165 (2023) 235.
[5] Y. Chen, F. Hu, Y.N. Hao, et al., Nano Res. 15 (2022) 3283.
[6] Y.N. Hao, Y.J. Sun, H. Wang, et al., Electrochim. Acta 449 (2023) 142213.
[7] M.J. Liu, Y.C. Wang, T.T. Yu, et al., Sci. Bull. 68 (2023) 1238.
[8] H.Y. Jing, P. Zhu, X.B. Zheng, et al., Adv. Powder Mater. 1 (2022) 100013.
[9] B.B. Wang, S.H. Chen, Z.D. Zhang, D.S. Wang, Smart Mat 3 (2022) 84.
[10] H.H. Ou, G.S. Li, W. Ren, et al., J. Am. Chem. Soc. 144 (2022) 22075.
[11] J.X. Wang, D.N. Deng, Q.M. Wu, et al., ACS Nano 17 (2023) 18653.

[12] X.J. She, Y.F. Wang, H. Xu, S.C.E. Tsang, S.P. Lau, Angew. Chem. Int. Ed. 61 (2022) e202211396.
[13] L.S. Zhan, Y.C. Wang, M.J. Liu, et al., Rare Met. 42 (2023) 806.
[14] X.H. Sun, L. Sun, G.N. Li, et al., Angew. Chem. Int. Ed. 61 (2022) e202207677.
[15] Y.C. Wang, L. Xu, L.S. Zhan, et al., Nano Energy 92 (2022) 106780.
[16] Y. Wang, X.B. Zheng, D.S. Wang, Nano Res. 15 (2022) 1730.
[17] L.G. Wang, J.B. Wu, S.W. Wang, et al., Nano Res. 17 (2024) 3261–3301.
[18] Q.C. Wang, Y.P. Lei, Y.C. Wang, et al., Energy Environ. Sci. 13 (2020) 1593.
[19] X. Zhao, M.J. Liu, Y.C. Wang, et al., ACS Nano 16 (2022) 19959.
[20] Y.C. Wang, Z.S. Huang, Y.P. Lei, et al., Chem. Commun. 58 (2022) 3621.
[21] H.C. Peng, J. Ren, Y.C. Wang, et al., Nano Energy 88 (2021) 106307.
[22] X. Zhao, Y.C. Wang, L.S. Zhan, et al., Chem. Commun. 58 (2022) 12716.
[23] H.B. Wang, C.Y. Tang, B. Sun, et al., Int. J. Extreme Manuf. 4 (2022) 035002.
[24] B.Q. Gao, Y. Pan, H. Yang, Appl. Catal. B: Environ. 315 (2022) 121580.
[25] L. Chen, C.Z. He, R. Wang, et al., Chin. Chem. Lett. 32 (2021) 53–56.
[26] J. Yu, A. Kudo, Adv. Funct. Mater. 16 (2006) 2163.
[27] L. Wang, J.X. Liu, W.Y. Song, et al., Chem. Eng. J. 366 (2019) 504.
[28] F.Q. Ma, J.W. Yao, Y.F. Zhang, Y. Wei, Chin. Chem. Lett. 29 (2018) 1689–1691.
[29] J.B. Pan, B.H. Wang, J.B. Wang, et al., Angew. Chem. Int. Ed. 60 (2021) 1433.
[30] Y.T. Wang, Y.H. Li, J.Z. Liu, et al., Angew. Chem. Int. Ed. 60 (2021) 7681.
[31] W.B. Wang, Z.T. Wang, R.O. Yang, et al., Angew. Chem. Int. Ed. 60 (2021) 22940.
[32] S. Liu, Y.P. Fan, Y. Wang, et al., Nano Lett. 22 (2022) 9107.
[33] J.Y. Duan, T.Y. Liu, Y.H. Zhao, et al., Nat. Commun. 13 (2022) 2039.
[34] Q.C. Wang, Q.G. Feng, Y.P. Lei, et al., Nat. Commun. 13 (2022) 3689.
[35] Y. Wang, J. Wu, C.L. Ye, et al., Angew. Chem. Int. Ed. 62 (2023) e202219191.
[36] T.T. Cui, Y.P. Wang, T. Ye, et al., Angew. Chem. Int. Ed. 61 (2022) e202115219.
[37] Q. Li, Y.C. Wang, J. Zeng, et al., Chin. Chem. Lett. 32 (2021) 3355–3358.
[38] K. Ye, G.R. Zhang, X.Y. Ma, et al., Energy Environ. Sci. 15 (2022) 749.
[39] Y.N. Hao, F. Hu, S.Q. Zhu, et al., Angew. Chem. Int. Ed. 62 (2023) e202304179.
[40] J.D. Yi, X.P. Gao, H. Zhou, W. Chen, Y.E. Wu, Angew. Chem. Int. Ed. 61 (2022) e202212329.